ELSEVIER

Contents lists available at ScienceDirect

# Ceramics International

journal homepage: www.elsevier.com/locate/ceramint





# The mechanism and machinability of laser-assisted machining zirconia ceramics

Zhelun Ma <sup>a,b,c</sup>, Qinghua Wang <sup>d</sup>, Yingdong Liang <sup>a,b</sup>, Zhijie Cui <sup>a,b</sup>, Fanwei Meng <sup>a,b</sup>, Liaoyuan Chen <sup>a,b</sup>, Zixuan Wang <sup>a,b</sup>, Tianbiao Yu <sup>a,b,\*</sup>, Changsheng Liu <sup>c,\*\*</sup>

- <sup>a</sup> Key Laboratory of High-end Equipment Intelligent Design and Manufacturing Technology, Liaoning Province, PR China
- <sup>b</sup> School of Mechanical Engineering and Automation, Northeastern University, Shenyang, PR China
- Ekey Laboratory for Anisotropy and Texture of Materials, Ministry of Education, School of Materials Science and Engineering, Northeastern University, Shenyang, China
- <sup>d</sup> School of Mechanical Engineering, Southeast University, Nanjing, PR China

#### ARTICLE INFO

# Keywords: Laser-assisted machining Absorptivity Mechanical property Plastic-brittle transition Zirconia ceramic

#### ABSTRACT

Laser-assisted machining (LAM) is regarded as a useful technique which can process ceramic materials without damage and efficiently. This work reported a study on the mechanism by which LAM technology can improve the machinability of zirconia ceramic. The absorptivity of zirconia ceramic to fiber laser energy was obtained through the combination of experiment and simulation. The temperature-dependent mechanical property of zirconia ceramic was studied by nanoindentation experiments. Meanwhile, scratch tests were used to investigate the plastic-brittle transition and damage mechanism under various high-temperature conditions. The results showed that the absorptivity of zirconia ceramic to fiber laser energy is 0.52. The hardness and elasticity modulus are decreasing as the temperature increases. The functions that relate them to temperature are fitted. Moreover, the increase in temperature can enhance the plastic-brittle transition depth of ceramic and suppress median cracks and chipping. Furthermore, the shape of the chips is changed from discontinuous lumpy chips to continuous coiled chips. These evidence and research can clearly explain the mechanism by which LAM technology can improve the machinability of zirconia ceramics. They can also provide guidance and theory for the industrialization of LAM technology.

# 1. Introduction

Zirconia ceramic is a typical hard and brittle material which is usually applied to aerospace, energy, and health fields [1–4]. However, due to its superior mechanical properties, it is difficult to machine with damage-free. Therefore, some combined machining methods such as vibration-assisted machining [5], chemistry-assisted machining [6,7], magnetic-assisted machining [8], minimum quantity lubrication machining [9–11], and thermal-assisted machining [12]. The mechanism of most above-mentioned machining methods is that the trajectory of the abrasive grit movement is changed to improve the surface integrity. However, the essential mechanism of thermal-assisted machining is that the mechanical properties of the workpiece are changed to make it easier to remove. So it can be regarded as one of the most promising processing methods. In recent years, since the cost of laser equipment has significantly decreased, laser source has supplanted

other common heat sources.

One of the main reasons why industrialization of thermal-assisted machining is difficult is that different materials absorb different amounts of heat source energy. Rozzi et al. [13,14] established a transient three-dimensional thermal model of a rotating cylindrical work-piece under the action of a translational laser source. Subsequently, Pfefferkorn et al. [15] extended this model to translucent homogeneous materials using LAM techniques and applied it to zirconia ceramic. Kalyanasundaram et al. [16] established the analytical model for stress and temperature fields in the workpiece during laser heating and waterjet quenching. Ding and Shin et al. [17] also established a three-dimensional transient thermal model for laser-assisted turning of hardened steel to predict the temperature field of hollow shafts with different thicknesses. Ren and Xu et al. [18] built a three-dimensional thermal model for the LAM process of fused silica, which was validated by experiments. Consequently, the temperature field modeling of

E-mail addresses: tianbiaoyudyx@gmail.com (T. Yu), csliu@mail.neu.edu.cn (C. Liu).

<sup>\*</sup> Corresponding author: Key Laboratory of High-end Equipment Intelligent Design and Manufacturing Technology, Liaoning Province, PR China.

<sup>\*\*</sup> Corresponding author.

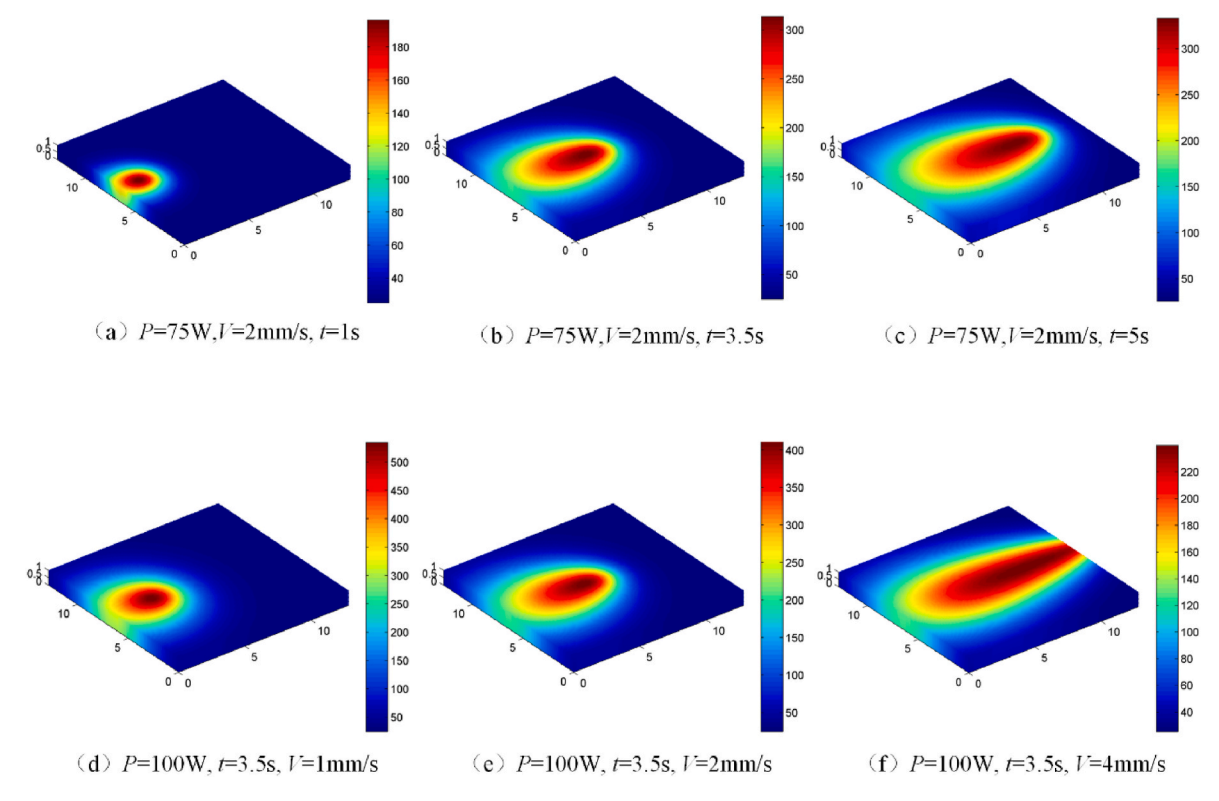


Fig. 1. The simulation of temperature distribution of zirconia ceramic surface with different laser parameter.

the LAM process had been fairly accurate, but little research on absorptivity of material and laser energy has been done, which seriously restricts the industrialization of LAM technology.

The mechanism of LAM process for ceramic materials has long been a focus of investigation. Kizaki et al. [19] built a laser-assisted grinding device and showed experimentally that LAM technology can reduce grinding forces and tool damage. Guo et al. [20] optimized the machining parameters during the LAM process, which the surface roughness of crystal silicon was reduced to 1.9 nm. Zhai et al. [21] studied the influence of fiber orientation of C/SiC composites by LAM. Wu et al. [22] applied the LAM technology to silicon nitride ceramics. The results showed that the micro-groove preparation by LAM could reduce the grinding force and improve the surface integrity. Li et al. [23] performed the molecular dynamics simulation of LAM for GaN single crystals. Additionally, we also have previously finished some work on laser-assisted grinding for efficient and high precision machining of zirconia ceramics [24-26]. However, most of these studies analyzed the superiority of LAM technology through experimental phenomena such as surface roughness, surface integrity and machining force. Little studies had been done about the mechanism which the LAM technology can improve the machinability of material from the perspective of temperature-dependent mechanical property of material.

In this paper, the absorptivity of zirconia ceramic to laser energy would be obtained via comparing experimental results and model simulations. The temperature-dependent mechanical properties of zirconia ceramic would be studied by nanoindentation tests. Meanwhile, the plastic-brittle transition and damage mechanism of zirconia ceramic under the various temperature condition would be explored through scratch tests. These studies would reveal the mechanism by which LAM technology can improve the machinability of zirconia ceramics. They can also provide guidance and theoretical support for the industrial application of LAM technology.

#### 2. Mechanism

During the laser-assisted machining process, temperature distribution by laser beam is a vital part for the study on machinability of the material. Since different material absorbs laser energy differently, the temperature distribution model is required, so the Fourier heat equation is employed and listed as follows:

$$\frac{\partial^2 T}{\partial x^2} + \frac{\partial^2 T}{\partial y^2} + \frac{\partial^2 T}{\partial z^2} + Q = \frac{1}{\alpha} \frac{\partial T}{\partial t}$$
 (1)

The Green's function is applied to calculate the temperature distribution, and the detailed derivation has been discussed in the previous studies [25]. So the final function of temperature distribution can be shown as follows:

$$T(x,y,z,t) = \sum_{i=n}^{(t-t_0)/\Delta t} \frac{2Q_{(t-t_0-i\Delta t)}}{\left[C_p \rho \left(4\pi\alpha \left(t-t_0-i\Delta t\right)\right]^{3/2}\right]} \cdot \exp\left[\frac{\left(x-x''-i\Delta t v_x\right)^2 + \left(y-y''-i\Delta t v_y\right)^2 + \left(z-z''-i\Delta t v_z\right)^2}{4\alpha \left(t-t_0-i\Delta t\right)}\right] (n=0,1,2,3...)$$
(2)

Where, T = T(x, y, z, t) represents the temperature distribution with respect to time t, Q is the laser beam energy,  $C_p$  is the specific heat,  $\alpha$  is the thermal diffusivity,  $t_0$  is the initial time, and  $\Delta t$  is the time cell.

Fig. 1 shows the simulation of temperature distribution under the different laser parameters. As time goes on, the highest temperature of workpiece surface is increasing, and the heat affected zone (HAZ) is expanding. When the time exceeds a threshold, the highest temperature no longer significantly increases, and a steady-state temperature field is formed (see Fig. 1a–c). Fig. 1d–f indicate the temperature distribution under the different moving speed of laser beam. As shown in it, as the increasing speed, the HAZ is also expanding, but the peak temperature is decreasing. Combined these simulations of temperature distribution, the rule of temperature distribution closely resembles the actual situation. It

 Table 1

 Laser parameters of temperature measurement experiments.

No.	Laser power (W)	Moving speed (mm/s)	Spanning length (mm)
1	75	1	30
2	75	2	30
3	100	1	30
4	100	2	30
5	100	3	30
6	100	4	30
7	125	1	30
8	125	2	30
9	125	3	30
10	125	4	30
11	150	1	30
12	150	2	30
13	150	3	30
14	150	4	30

should be noted that the absorptivity of laser energy is assumed as 1 during the simulated process, whereas ti is impossible during the actual thermal process. Therefore, the absorptivity would be investigated using the combination of experimental and theoretical methods.

#### 3. Method

#### 3.1. Measurement of temperature distribution

The experimental specimens are 3Y-TZP (3 mol%Y $_2O_3$ ), which made in WeiJia Company (China). The size is 40mm  $\times$  30mm  $\times$  3 mm. A fiber laser system which made in IPG Company (the laser spot is 2 mm) is employed to offer the laser energy. The 600 K infrared thermal imager is used to measure the temperature distribution. The measured range is 0–650 °C, the thermal sensitivity is 0.05 °C, the accuracy is  $\pm 2$  °C, and the temperature measurement pixel is 384  $\times$  288. The detector is an uncooled infrared focal plane detector, the response band is 8–12  $\mu m$ , and the sampling frequency is 50 Hz. Each group of experiment was measured three times, and the absorptivity would be obtained by comparing the simulated and experimental results. The detail experimental plan can be found in Table 1.

## 3.2. Nanoindentation test

To investigate the mechanical properties of zirconia ceramics at room temperature and high temperature conditions, nanoindentation experiments were carried out using the Berkovich tip on a Nona Test measurement system which produced by Micro Materials (shown in Fig. 2b). This system has a loading range of 0–500 mN and a testing temperature range of -30-500 °C. The size of specimen is 6mm  $\times$  6mm  $\times$  3 mm. The surface of the specimen is polished to less than 5 nm by mechanical polishing (to the extent that a mirror effect appears on the

surface). Before the experiments are implemented, the equipment needs to be position-calibrated so that the thermal drift of the measurement system is less than 0.3 nm. Fig. 2b shows the nanoindentation equipment in this paper, and the nanoindentation test is listed as Table 2.

#### 3.3. Scratch test

The scratch tests at room temperature were carried out on an MFT-4000 friction and wear tester, with an HRC-3 Rockwell diamond indenter. The tip radius is approximately 200  $\mu m$ , and the angle is approximately 120°. The size of zirconia ceramic specimen is 40mm  $\times$  30mm  $\times$  3 mm. Before the experiments began, the surfaces of the specimens were also polished to less than 20 nm of surface roughness. Fig. 3a and b shows the equipment for scratching test at room temperature. SEM and laser scanning confocal microscope were utilized to observe and measure the plastic-brittle translation depth and damage.

The scratch tests at high temperature were proposed on a 5-asix CNC machine tool with an accuracy of 0.1  $\mu m$ . The specimen was placed on a heating equipment and fixed by a specific clamp. One side of specimen would directly touch with the heating unit, and another side of the specimen would be scratched. The upper temperature of heating unit is 400  $^{\circ} \text{C}.$  When the set temperature is attained, the specimen should be held for 10–15 min to guarantee it to be properly heated, and then the specimen would be measured using a handheld infrared thermometer. Fig. 3c–g shows the detail process of high-temperature scratch test. The specimens need to be finely polished for 4 h before the experiment, the purpose of which is to remove the original defects of the zirconia ceramic.

# 4. Results and discussions

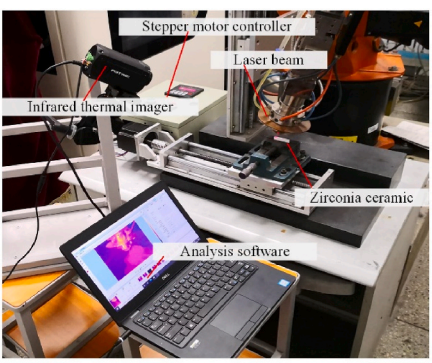
# 4.1. Absorptivity of laser energy

# 4.1.1. The effect of laser moving speed on absorptivity

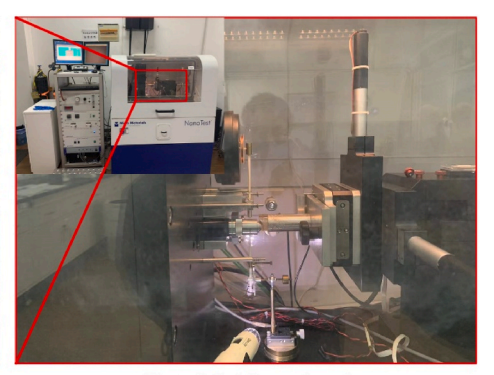
Due to the excessive data of temperature, in each group of experiments, the highest temperature in the temperature field at a certain moment is chosen as the object of study. The absorptivity in the simulation program is continuously adjusted so that the highest temperature of simulated temperature field has a good agreement with that of the

**Table 2**The parameters of nanoindentation test.

Parameters	Value
Temperature (°C)	25, 100, 200, 300, 400, 500
Loading force (mN)	0.5, 1, 2, 10, 20, 40, 60, 100, 200, 350, 500
Loading time (s)	10
Dwell time (s)	15
Unloading time (s)	10

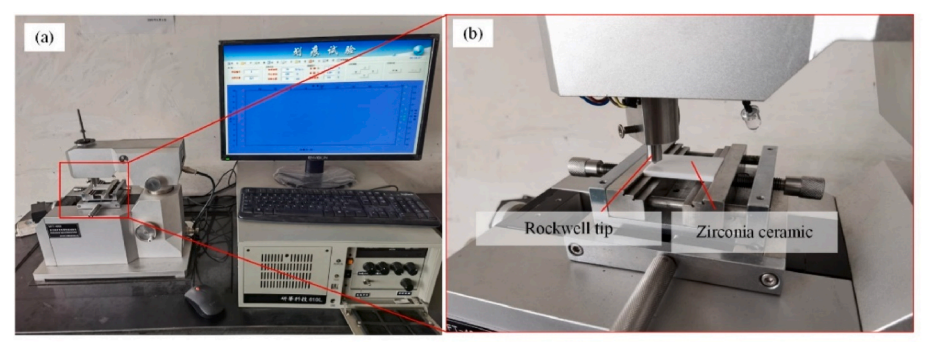


(a) temperature measurement

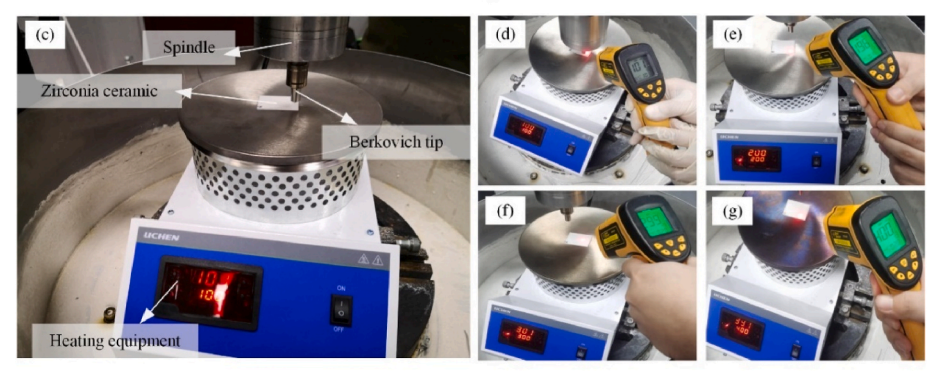


(b) nanoindentation equipment

Fig. 2. Experimental equipments in this paper.



Scratch test under room temperature condition



Scratch test under different temperature condition

Fig. 3. Scratch equipment.

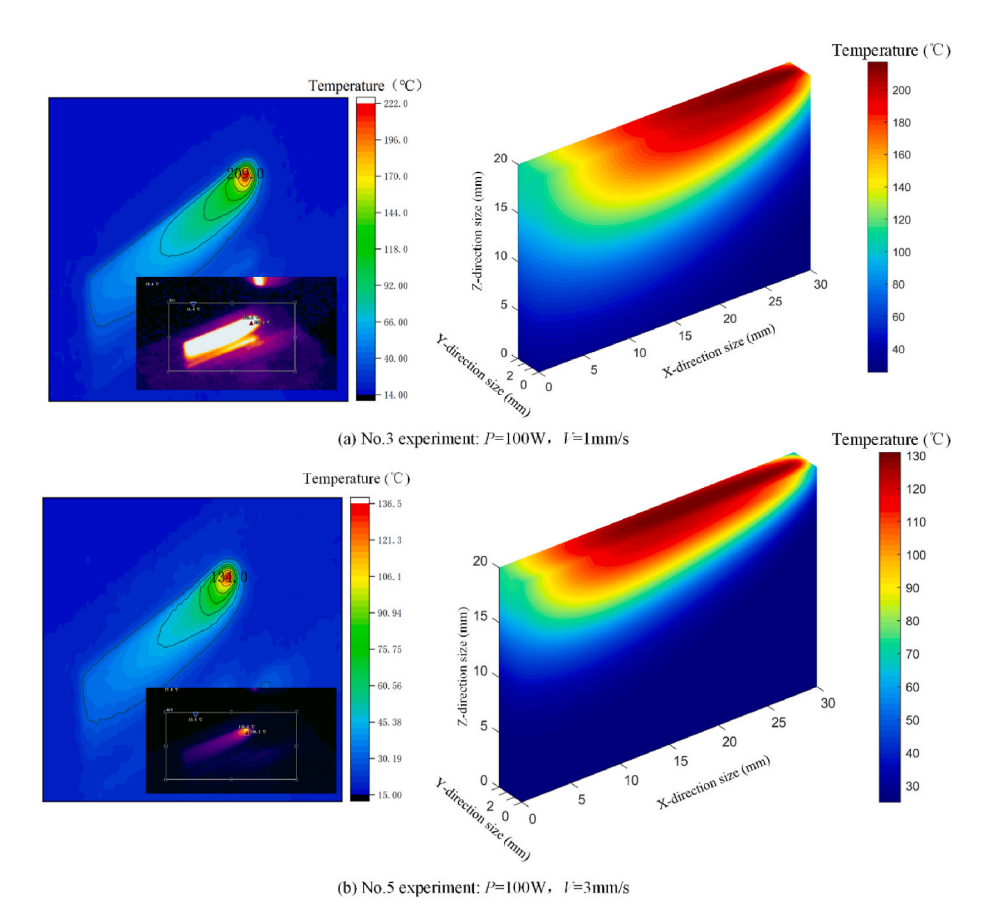


Fig. 4. The comparison between measured temperature field and simulated temperature field with different moving speed.

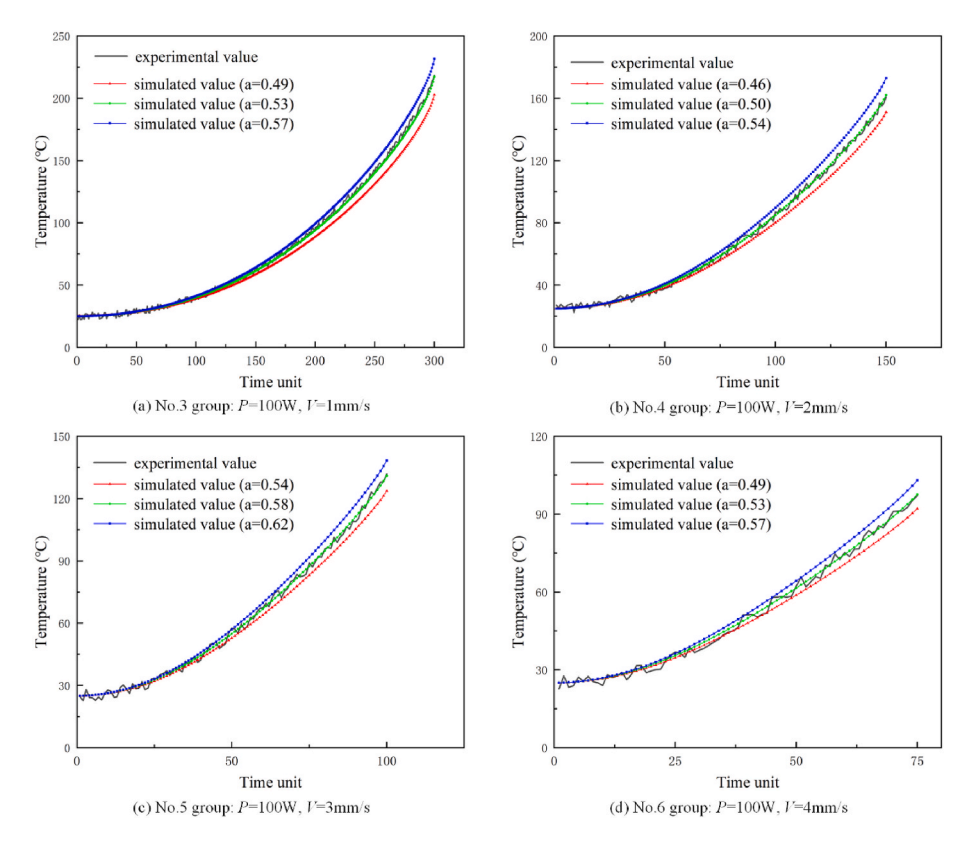


Fig. 5. Comparison between the highest experimental temperature and the highest simulated temperatures with different absorptivity.

actual temperature field.

Fig. 4 shows the comparison between measured temperature field and simulated temperature field with different moving speed. The moment of measurement is the moment when the laser is about to leave the workpiece surface. In the actual temperature field (in Fig. 4a), when the laser is about to leave the surface of workpiece, the highest temperature at this moment is 221.2  $^{\circ}$ C. In the simulated temperature field, when the absorptivity is adjusted to 0.53, the highest temperature at the same moment is 217.19  $^{\circ}$ C, and the error rate is only 1.8%. So 0.53 can be considered as the absorptivity because the simulated temperature has a good agreement with the actual temperature. In Fig. 4b, the highest temperatures of measurement and simulation are 134.0  $^{\circ}$ C and 130.8  $^{\circ}$ C, respectively. 0.58 is the suitable absorptivity for No.5 experiment group, and the error rate is 2.39% at this moment.

However, the absorptivity obtained by comparing only the highest temperature at a given moment is not representative. To improve the accuracy of the absorptivity, the highest temperatures of the measurement and simulation would be compared as a time interval of 0.1s. The highest temperatures of the whole process of laser sweeping over the surface of the workpiece are extracted, and the highest temperature variation is calculated under the different absorptivity, the detail results can be found in Fig. 5. As shown in Fig. 5a, in the initial stage, the variation of highest temperature at different absorptivity is inconspicuous, and it is basically consistent with the measured temperature. As time going by, the highest temperature within each time unit gradually creates a difference and the error rate between changes significantly. When the absorptivity is 0.49 and 0.57, the simulated highest temperature at each time unit obviously deviates from the measured temperature. When the absorptivity is 0.53, the simulated highest temperature in each time unit is in good agreement with the measured temperature. Therefore, this absorptivity can be regard as the suitable value under the given machining parameter. In the same way, the suitable absorptivity under the different moving speed is analyzed.

It is worth noting that there are fewer data due to the increase of

**Table 3**Comparison of the error rate between measured highest temperature and simulated highest temperature with different absorptivity under different moving speeds.

No.	Value					
3	Absorptivity	0.49	0.51	0.53	0.55	0.57
	Error rate	6.06%	4.22%	3.05%	3.87%	4.54%
4	Absorptivity	0.46	0.48	0.50	0.52	0.54
	Error rate	5.23%	4.23%	3.07%	4.89%	5.67%
5	Absorptivity	0.54	0.56	0.58	0.60	0.62
	Error rate	4.91%	3.78%	3.28%	4.28%	5.03%
6	Absorptivity	0.49	0.51	0.53	0.55	0.57
	Error rate	4.46%	4.08%	3.59%	4.66%	5.60%

moving speed, which would make the simulated temperature value and the measured temperature value have a large error, so this paper continues to analyze the error rate at each absorption rate in detail.

Table 3 shows the comparison of the error rate between measured highest temperature and simulated highest temperature with different absorptivity. The error rate of each time unit was calculated, and the average error rate is listed as Table 3. After calculating the error rate using different absorptivity, a suitable absorptivity with a minimum error rate can be obtained for each processing condition. The results showed that the absorptivity is about 0.50–0.58, and there is no obvious linear relationship with the laser moving speed. The error rate is controlled within 4%, the minimum can reach about 3%.

# 4.1.2. The effect of laser power on absorptivity

Fig. 6 shows that the comparison of actual and simulated highest temperature with different absorptivity under the different laser power. As shown in Fig. 6a, the highest temperature is  $88.3\,^{\circ}\text{C}$  in the entire process. At this moment, when the absorptivity is adjusted as 0.47, the simulated highest temperature is  $87.7\,^{\circ}\text{C}$ , the error rate is minimized. The highest temperature varies in line with the increase in laser power.

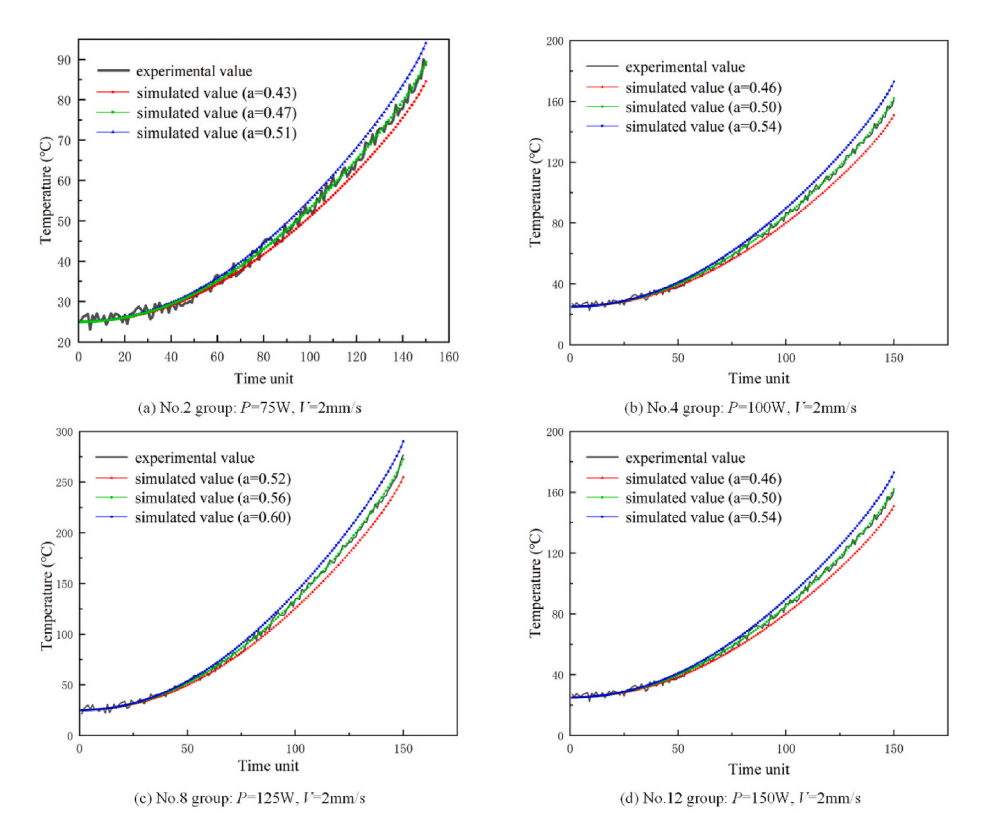


Fig. 6. Comparison between the measured highest temperature and the simulated highest temperature with different absorptivity.

**Table 4**Comparison of the error rate between measured highest temperature and simulated highest temperature with different absorptivity under different laser powers.

No.	value					
2	Absorptivity	0.43	0.45	0.47	0.49	0.51
	Error rate	4.12%	3.77%	3.28%	3.87%	4.25%
4	Absorptivity	0.46	0.48	0.50	0.52	0.54
	Error rate	5.23%	4.23%	3.07%	4.89%	5.67%
8	Absorptivity	0.52	0.54	0.56	0.58	0.60
	Error rate	6.95%	5.84%	4.61%	5.67%	6.25%
12	Absorptivity	0.49	0.51	0.53	0.55	0.57
	Error rate	9.33%	7.88%	6.60%	8.06%	9.17%

The range of suitable absorptivity is from 0.47 to 0.56, so the detail analysis on the error rate of temperature in each time unit under the different absorptivity would be studied.

Table 4 lists the comparison of the error rate between measured highest temperature and simulated highest temperature with different absorptivity under different laser powers. When the different absorptivity is calculated, the error rate in each group of experiments showed a trend of decreasing and then increasing, so the most suitable absorptivity in each group of experiments can be found, and its variation range is 0.47–0.56, and there is no obvious trend relationship between the absorptivity and the laser power. Therefore, it can be considered that the absorptivity of material to laser energy is independent of laser power.

It is worth noting that the error rate becomes significantly larger with the laser power increasing. When the laser power is low (P=75~W and P=100~W), the error rate is not significant. When the laser power continues to increase (P=125~W and P=150~W), the surface temperature

**Table 5**Statistics of absorptivity of laser-zirconia reaction, measured highest temperature and error rate.

No.	The first experime	The first experiment			The second experiment		
	Absorptivity	Error rate	Highest temperature (°C)	Absorptivity	Error rate	Highest temperature (°C)	
1	0.49	3.45%	145.2	0.52	3.09%	157.1	
2	0.47	3.28%	75.0	0.51	3.55%	79.3	
3	0.53	3.05%	218.8	0.49	3.74%	211.6	
4	0.50	3.07%	161.4	0.54	3.22%	174.4	
5	0.58	3.28%	130.9	0.54	3.65%	141.9	
6	0.53	3.59%	97.1	0.56	4.03%	104.8	
7	0.52	4.98%	334.7	0.55	4.87%	351.7	
8	0.58	4.61%	276.8	0.53	4.58%	256.4	
9	0.56	4.12%	210.4	0.51	3.47%	222.5	
10	0.57	3.77%	154.1	0.55	3.21%	161.3	
11	0.48	7.08%	620.4	0.50	6.11%	635.1	
12	0.53	6.60%	457.7	0.49	6.58%	448.4	
13	0.51	5.18%	327.4	0.47	4.76%	313.9	
14	0.45	4.55%	194.6	0.50	5.13%	185.6	
Average	0.5214	4.33%	_	0.5186	4.29%	-	

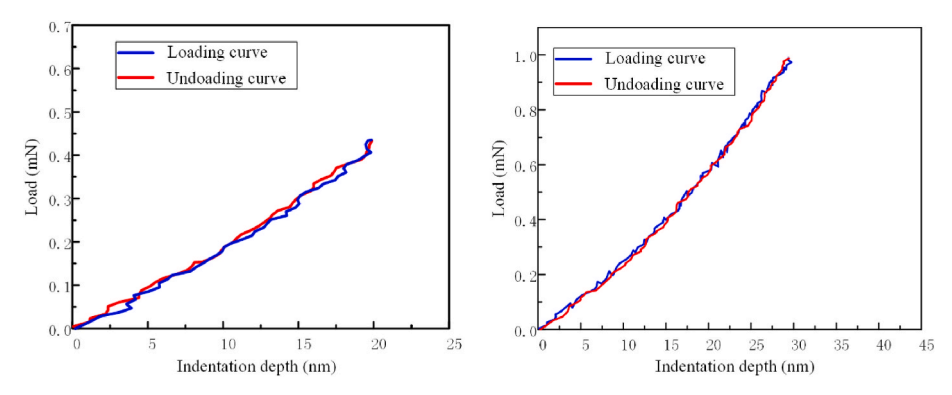


Fig. 7. Depth-load curve where elastic deformation occurs.

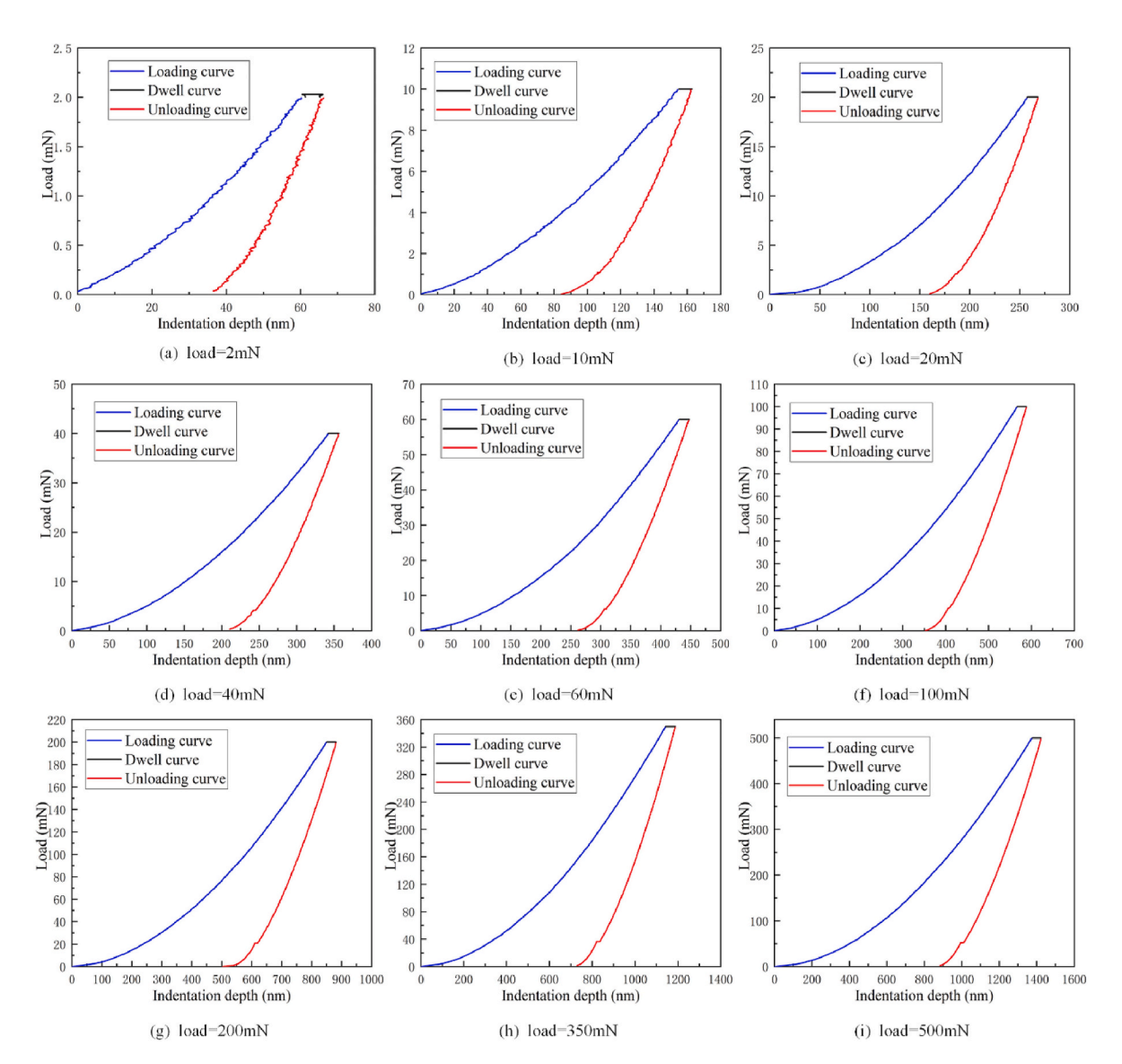


Fig. 8. Depth-load curves for different normal load s at room temperature.

of the swept workpiece increases significantly, resulting in excessive temperature difference with the environment temperature. The temperature jump is too large, and the error rate between the measured highest temperature and the simulated highest temperature becomes larger compared with that at low laser power, and its error range is increased from 3.07%-5.67% to 4.61%–9.33%.

# 4.1.3. Absorptivity statistics

After analyzing the effect of laser moving speed and laser power on the absorptivity, the value for the absorptivity of zirconia ceramic to the laser energy needs to be found. To improve the accuracy of calculation, the absorptivity under the given processing condition was measured and calculated for each group of experiments in this paper. And each group

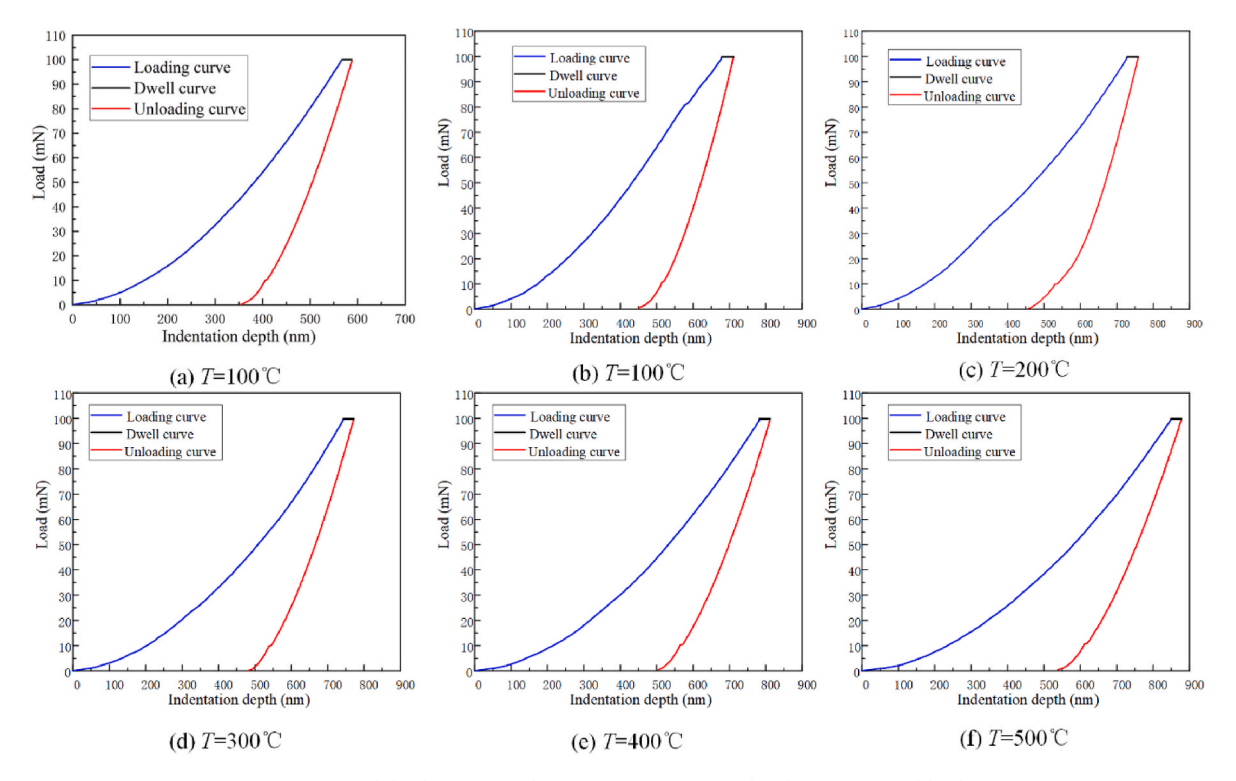


Fig. 9. Depth-load curves for different temperatures under the same normal load.

of experiments was measured twice, and the average value was taken as the final measured laser energy absorptivity.

Table 5 shows the statistics of absorptivity, error rate and highest temperature. As shown in it, regardless of the variation of the processing parameters, the absorptivity in each group of experiments ranged from 0.45 to 0.58 with an error rate of 3.05%–7.08%. After several measurements and evaluations, the average absorptivity was 0.52. This absorptivity can provide some guidance for laser-assisted machining of zirconia ceramics processes.

# 4.2. Temperature-dependent property of zirconia ceramic

# 4.2.1. Stress-strain analysis

Stress-strain curves reflect the various deformation processes such as brittleness, plasticity, yielding and fracture of materials under the action of external forces. The depth-load curves of the elastic deformation occurring during the nanoindentation using the Boehner indenter are shown in Fig. 7. When the indentation load is 0.5 mN and 1 mN, the zirconia ceramic deforms elastically. In the elastic deformation, the loading curve and unloading curve are almost coincident. After the

indenter presses into the zirconia ceramic, the zirconia molecules become denser with each other, and the molecular bonds do not break during the whole process, and then return to the original state after the indenter is unloaded.

As the load increases, the zirconia ceramic successively undergoes elastic deformation and plastic deformation stages. At this time, the load exceeds the yield stress of the zirconia ceramic. During the plastic deformation stage, the zirconia molecular bonds are broken and cannot be recovered, so the zirconia ceramics cannot recover their original shape during the unloading of the indenter. Fig. 8 shows the depth-load curves for different normal loads at room temperature. When the load is 2 mN, the zirconia ceramic already starts to deform plastically. Therefore, it can be considered that the critical normal load for plastic transformation is 1–2 mN. As the load gradually increases from 2 mN to 500 mN, the pressed depth and the indentation depth both increase continuously, but the relationship is not simply linear.

Fig. 9 shows the depth-load curves for different temperatures under the same normal load. When the normal load is uniformly 100 mN, at room temperature condition, the pressed depth is 588 nm and the indentation depth is about 352 nm; as the temperature rises to  $100 \, ^{\circ}\text{C}$ 

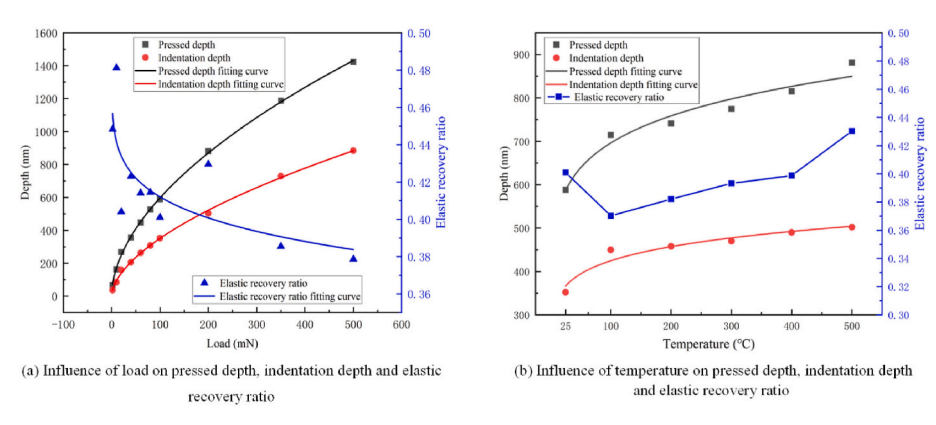


Fig. 10. The fitting results of pressed depth, indentation depth and elastic recovery ratio.

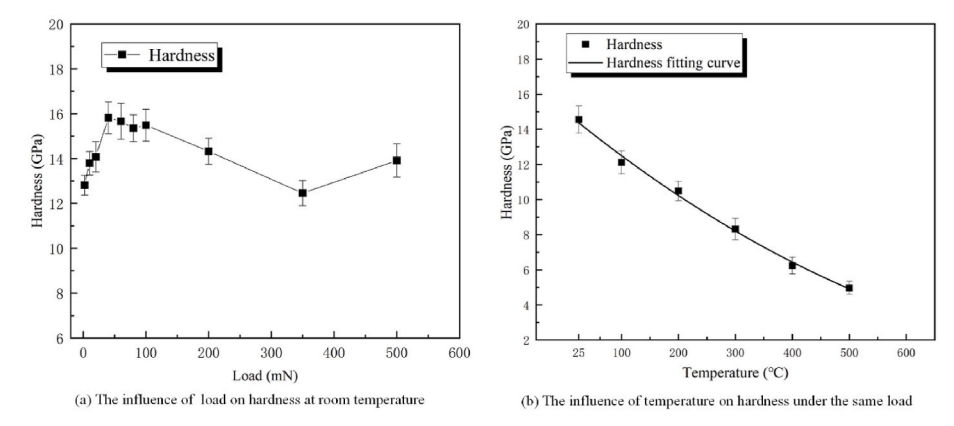


Fig. 11. The results of hardness variation under different conditions.

and 200 °C, the pressed depth continues to increase and reaches 714 nm and 745 nm respectively, while the indentation depth is similar, 450 nm and 458 nm respectively; However, when the temperature reaches 300 °C, the pressed depth is 774 nm and the indentation depth is about 470 nm; when the temperature reaches 400 °C, the pressed depth is 815 nm and the indentation depth is about 490 nm; when the temperature reaches 500 °C, the pressed depth is 881 nm and the indentation depth is about 502 nm. Compared with that under the room temperature condition, the pressed depth increased by 49.8% and the indentation depth increased by 42.6%. In summary, under the same load condition, the increase in temperature changes the mechanical properties of the workpiece material, making the material more susceptible to deformation.

#### 4.2.2. Elastic recovery ratio

Elastic recovery rate is a vital indicator for analyzing material properties in nanoindentation experiments. The calculation method is listed:

$$\eta = \frac{h_t - h_r}{h_t} \times 100\% \tag{4a}$$

Where,  $\eta$  is the elastic recovery rate,  $h_t$  is the pressed depth,  $h_r$  is the indentation depth.

The relationship between load and  $\eta$ ,  $h_b$   $h_r$  is shown in Fig. 10a. As the load increases, both  $h_t$  and  $h_r$  increase as a power function. So the power function is fitted, and the results are as follows:

$$h_t = 48.83668 \times P^{0.54335} \tag{4b}$$

$$h_r = 24.84702 \times P^{0.57468} \tag{5}$$

The elastic recovery ratio can be calculated as follows:

$$\eta = (1 - 0.50878 \times P^{0.03113}) \times 100\% \tag{6}$$

The fitting curve also can be found in Fig. 10a. It is worth noting that a small part of the elastic recovery rates has large differences with the fitted curve. It can be attributed to the size effect of nanoindentation. Most experimental values are following the fitting curve, which can better represent the trend between the load and depth.

Fig. 10b shows that the relationship between the temperature and  $\eta$ ,  $h_b$ ,  $h_r$ . Under the same load, the relationship between  $h_b$ ,  $h_r$  and temperature also can be considered to be increasing as a power function trend, the results are listed as follows:

$$h_t = 394.0734 \times T^{0.1236} \ (25^{\circ}C < T < 500^{\circ}C)$$
 (7)

$$h_r = 260.0577 \times T^{0.1065} \ (25^{\circ} C \le T \le 500^{\circ} C)$$
 (8)

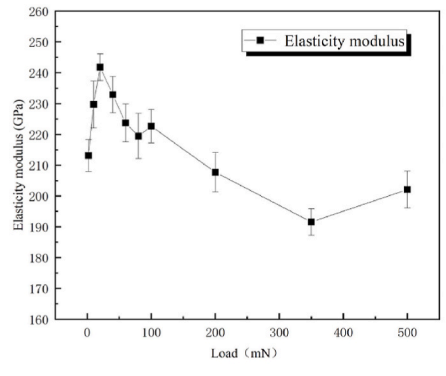
The elastic recovery ratio can be calculated as follows:

$$\eta = (1 - 0.65992 \times T^{0.0171}) \times 100\% \ (25^{\circ}C \le T \le 500^{\circ}C)$$
 (10)

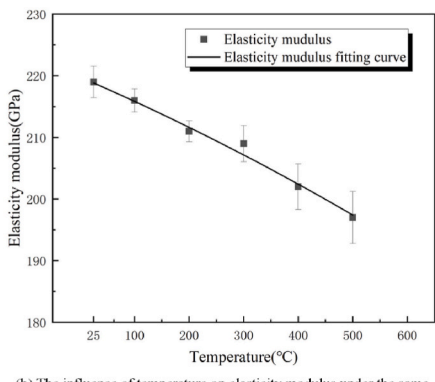
# 4.2.3. Hardness

The hardness of material is an important indicator, which reflect the ability to resist deformation. Fig. 11a shows the influence of load on hardness at room temperature. As shown in it, when the load is less than 60 mN, the measured hardness increases with the load raises; when the load exceeds 60 mN, the measured hardness would keep stable with the increasing load. It can be considered that there is no obvious correspondence between the hardness and load.

Fig. 11b indicates the influence of temperature on hardness under the same load. As the temperature rises, the hardness of zirconia ceramics is constantly decreasing. At room temperature, the hardness of zirconia is approximately 14.56 GPa, while at  $500\,^{\circ}\text{C}$  it decreases to  $4.9\,^{\circ}$ 



(a) The influence of load on elasticity modulus at room temperature



(b) The influence of temperature on elasticity modulus under the same load

Fig. 12. The fitting results of elasticity modulus under different conditions.

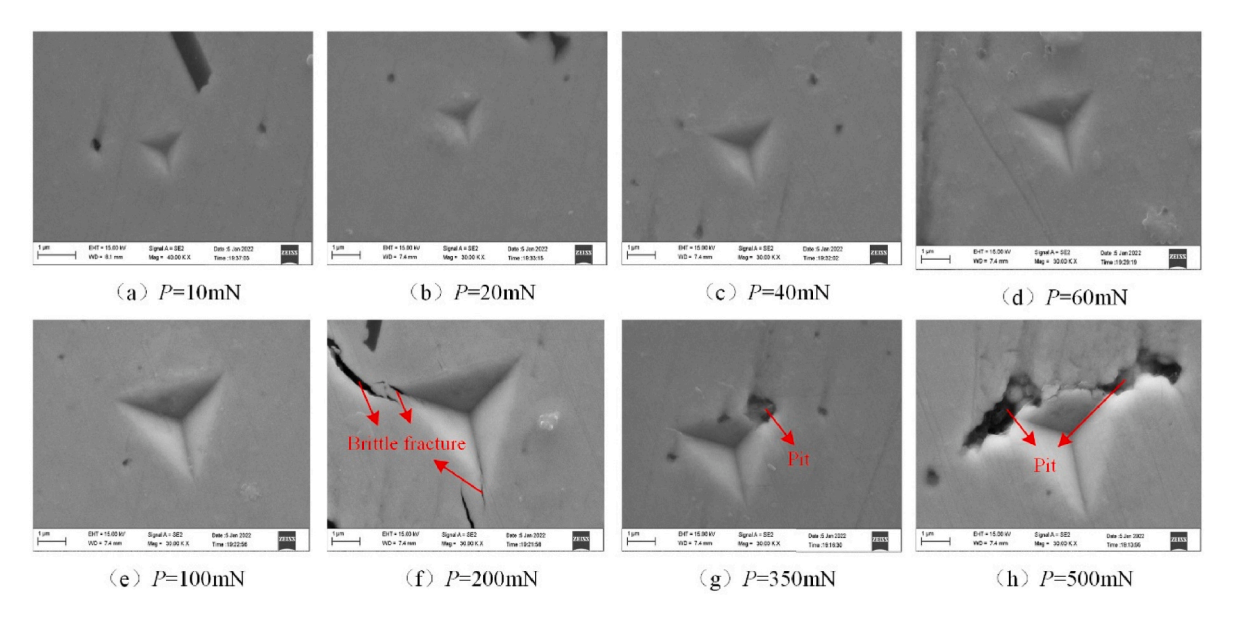


Fig. 13. SEM images of the nanoindentation morphology of zirconia ceramics under the different loads.

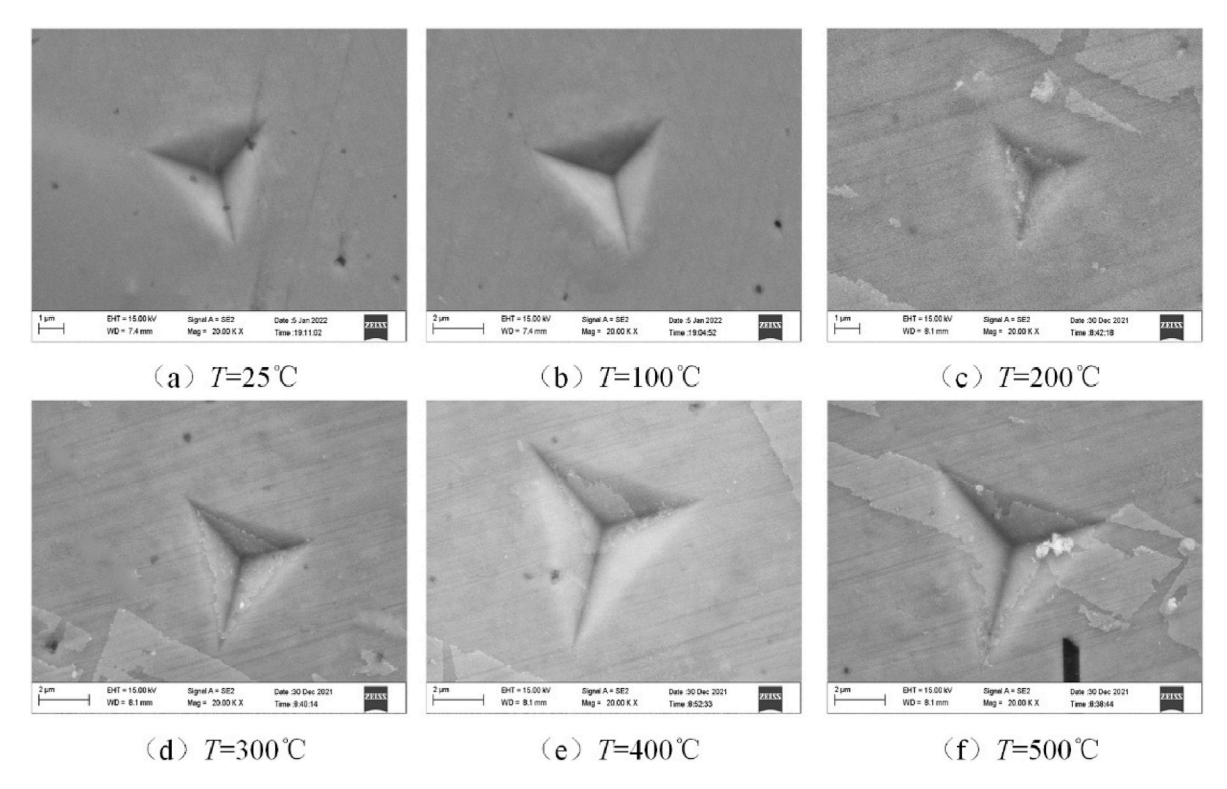


Fig. 14. SEM images of the nanoindentation morphology at the different temperatures under the same load.

GPa, a drop of 65.9%, which is a significant effect. The fitting function is calculated as follows:

$$H_v = 1.2498 \times 10^{-5} T^2 - 0.02645 T + 15.02$$
 (11)

# 4.2.4. Elasticity modulus

Elasticity modulus is a mathematical description of the tendency of an object to deform when an external force is applied to it. Fig. 12a shows the influence of the load on elasticity modulus at room temperature. When the load is less than 100 mN, the elasticity modulus tends to increase with the load increases. As the load continues to increase, the elasticity modulus decreases and stabilizes. In general, although there are some fluctuations in the measured value of elasticity modulus duo to

the different loads, the range is from 200 GPa to 240 GPa.

Fig. 12b indicates the influence of the temperature on elasticity modulus at the same load. As shown in it, As the temperature rises, the elasticity modulus of zirconia ceramics decreases gradually. The measured value of elasticity modulus at room temperature is 219 GPa, while the elasticity modulus drops to 196 GPa at 500  $^{\circ}\text{C}$  condition, a decrease of approximately 10.05%. The relationship between temperature and elasticity modulus of zirconia ceramics is obtained by fitting a polynomial to the measured elasticity modulus values at different temperatures, which can be expressed as:

$$E = -1.32509 \times 10^{-5} T^2 - 0.03817T + 219.80$$
 (12)

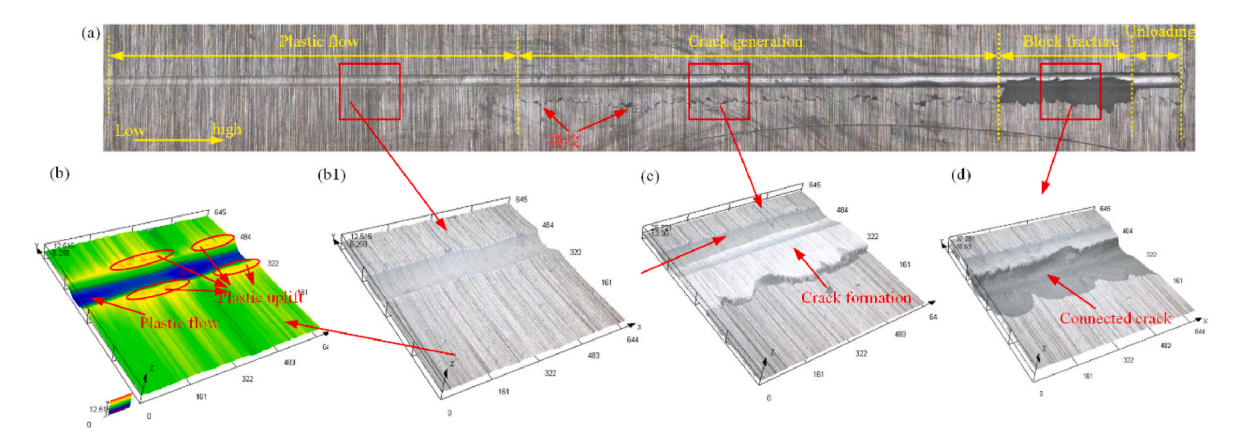


Fig. 15. The entire scratch morphology of zirconia ceramic.

# 4.2.5. Nanoindentation morphology

Fig. 13 shows the SEM images of the nanoindentation morphology of zirconia ceramics under the different loads obtained using a Berkovich tip. It can been seen that when the load is small, the size of indentation is also small and plastic flow of the material occurs. As the load increases, the size of the indentation gradually increases, indicating that the contact area between the material and indenter is increasing due to the plastic deformation. When the load is 200 mN (as shown in Fig. 13f), some cracks were generated at the indentation boundary. This is attributed to that the plastic flow is no longer able to resist the stress concentration, the brittle fracture begins to occur. When the load continues to increase to 350 mN (see Fig. 13g), the size of indentation remains essentially unchanged. But the collapse occurred at the boundary of indentation due to the excessive load and expansion of the cracks formed in the indentation zone, some of which extend to the surface of the material and create pits. When the load reaches 500 mN, the zone around the indentation had begun to break up considerably, and brittle fractures has completely taken over.

Fig. 14 shows the SEM images of the nanoindentation morphology at the different temperatures under the same load. As shown in it, compared with that at 25 °C, the size and morphology of indentation at 100 °C is essentially same. But the edges of indentation are more cleanly defined, indicating that the ability of the zirconia ceramic to deform plastically is increasing at this time. When the temperature reaches 200 °C, the size of indentation becomes large, the material is removed by the action of the indenter, forming the chips and being pressed into the zone of indentation. As the temperature continues to raise (350 °C and 500 °C), this phenomenon is becoming more and more evident, even lumpy chips of zirconia ceramics is formed. The size of indentation is also becoming larger. Consequently, the increase in temperature leads to a variation in the mechanical properties of zirconia ceramic, making it

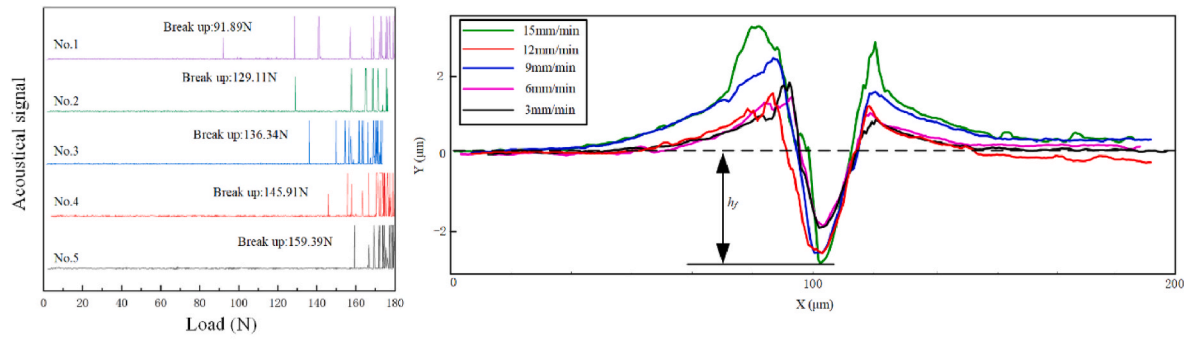
easier for plastic deformation to occur, and the material would be more easily removed.

# 4.3. Plastic-brittle transition and damage mechanism

The removal mode of hard and brittle material has been a hot topic of research. In 1991, Bifano [27] first introduced the concept of plastic-region machining technology for hard and brittle materials. The main issue of plastic-region machining is that the plastic region of most hard and brittle materials is at the nanoscale, leading to the extremely low efficiency in the machining process [28]. Therefore, if the plastic region could be increased, the machining efficiency would be substantially improved. In the ductile-brittle transition model proposed by Bifano, the mechanical properties of the material (fracture toughness, elasticity modulus, and hardness) together determine the critical chip-forming thickness in plastic-region machining process. So in this section, the plastic-brittle transition and damage mechanism under the different temperature conditions would be analyzed and discussed.

# 4.3.1. At room temperature condition

Fig. 15 shows the entire scratch morphology of zirconia ceramic. The indenter moves from left to right at a certain speed and the load increases linearly in the normal direction, and then the load is unloaded after it reaches the set value. As shown in it, zirconia ceramic is divided into three stages during the entire scribing process: the plastic flow stage, the crack generation stage, and the block fracture stage. At the initial stage, the material is removed with the plastic flow mode. The phenomenon of plastic uplift can be observed (see Fig. 15b-b1). Subsequently, the crack is generated due to the compression of the indenter. But these cracks are not connected to each other. When the load exceeds a threshold, a large number of cracks interconnect and the material



(a) The result of acoustical signal measurement and critical loading

(b) The comparison of the depth of plastic-brittle transition at different scratch speeds

Fig. 16. The results of plastic-brittle transition.

**Table 6**The experimental parameters in the scratch test at room temperature.

No.	load	Loading speed (N/ min)	Scratch length (mm)	Scratch speed (mm/min)	Scratch depth (µm)	Scratch width (µm)
1	180	18	30	3	1.803	17.875
2	180	36	30	6	1.842	18.5
3	180	54	30	9	2.345	18.75
4	180	72	30	12	2.401	18.75
5	180	90	30	15	2.612	13.875

begins to spall, forming a brittle fracture where the area of brittle fractures is much larger than that of the indenter action.

Fig. 16a shows the first brittle fracture result of zirconia ceramic using acoustical signal measurement. As the scratching speed increases, the load at which the first breakage of the zirconia ceramic occurs increases continuously. The reason can be attributed to the fact that the increase in scratching speed leads to an increase in the strain rate of the material, the average contact stress between the material and indenter becomes greater, and the critical load for its breakage to occur with little change in contact area is also greater for the strain.

Fig. 16b and Table 6 show the comparisons of plastic-brittle transition depth and scratch width with different scratch speeds. As shown in them, under the room temperature condition, the plastic-brittle transition depth tends to increase with the increase of loading speed. When the scratching speed reaches 3 mm/min, the critical depth is the smallest, which is 1.803 μm; when the scratching speed reaches 15 mm/min, the critical depth reaches the maximum, is 2.612 µm. In terms of scratch width, except that the scratch width is obviously smaller than other scratches when the scratch rate is 15 mm/min, the width of other scratches is basically unchanged. As can be observed, with the increase of scratching speed, although the depth of plastic-to-brittle transition tends to increase, the width of the scratch does not change, indicating that the indenter has not substantially completely pressed into the interior of the zirconia ceramic. The increase of scratching speed cannot substantially improve the plastic-brittle critical depth of zirconia ceramics.

# 4.3.2. At high temperature condition

Fig. 17 and Table 7 show the sectional curves in the plastic-brittle region, scratch depth and scratch width under the different temperature condition. As show in Fig. 17, When the temperature is  $100\,^{\circ}$ C, the depth of plastic-brittle transition is small, and the plastic uplifts on both sides of the scratch are also less; as the temperature rises, the depth of plastic-brittle transition increases continuously, and the plastic uplifts on both sides also increase. When the temperature reaches  $400\,^{\circ}$ C, the plastic uplift on both sides of the scratch is obviously higher than that at other temperatures, and the depth of plastic-brittle transition also increases significantly. This indicates that the increase in temperature makes zirconia ceramics more likely to undergo plastic deformation, and

the increase in the depth of plastic-brittle transition also means that the depth where brittle fracture would have occurred has changed to plastic flow under the action of temperature. This also proves that increasing the processing temperature of zirconia ceramics is beneficial to realize the plastic-region machining of zirconia ceramics.

When the temperature increased from 100  $^{\circ}\text{C}$  to 400  $^{\circ}\text{C}$ , the scratch width did not change much, only increased by 8.19%, but the depth of plastic-to-brittle transition increased by 25.1%. Compared with room temperature, the scratch width is not comparable due to the difference in experimental equipment. But the depth of plastic-brittle transition has increased by 25%. LAM can significantly improve the plastic region of zirconia ceramic, which can greatly improve the machining efficiency while guaranteeing processing accuracy.

Fig. 18 shows the SEM image of scratch morphology of zirconia ceramics at different temperatures. In order to observe the morphology of each stage of the scratch, a section at the front, middle and end of each scratch would be selected, and it would select the same position for scratches at different temperatures to observe the influence of temperature on the scratch morphology. As shown in Fig. 18a, in the plastic removal stage (see Fig. 18a1), there is no damage in the scratch zone. As the indenter continues to press down, the pits appear intermittently, and the median cracks also can be observed, indicating that brittle fracture has occurred on both sides. The indenter continues to press down, many pits and cracks appear, and the removed zirconia ceramics are blocky and discontinuous. When the temperature is 200 °C (see Fig. 18b), there is no significant change in the plastic removal stage, and the size of the pits decreases in the plastic-brittle transition stage, the length of the median crack is also reduced (see Fig. 18b2). In the brittle fracture zone, there is no obvious difference from the morphology at 100 °C, and it is also dominated by many pits and brittle fractures, accompanied by many median cracks, and the removed zirconia ceramics are still in the form of blocks (see Fig. 18b3).

When the temperature rises to 300  $^{\circ}$ C (see Fig. 18c), the plastic removal stage still has no obvious change. But in the plastic-brittle transition stage, although there are still pits, their size and number had been significantly reduced compared with the previous ones. In the brittle fracture stage, the size of the pits continues to decrease, but the size of the cracks does not change much. When the temperature reaches 400  $^{\circ}$ C, the plastic uplift on both sides of the scratch is more obvious,

**Table 7**The experimental parameters in the high-temperature scratch test.

No.	Temperature (°C)	Scratch length (mm)	Scratch speed (mm/ min)	Scratch depth (µm)	Scratch width (μm)
6	100	30	6	3.674	78.64
7	200	30	6	3.975	81.21
8	300	30	6	4.142	84.76
9	400	30	6	4.598	85.08

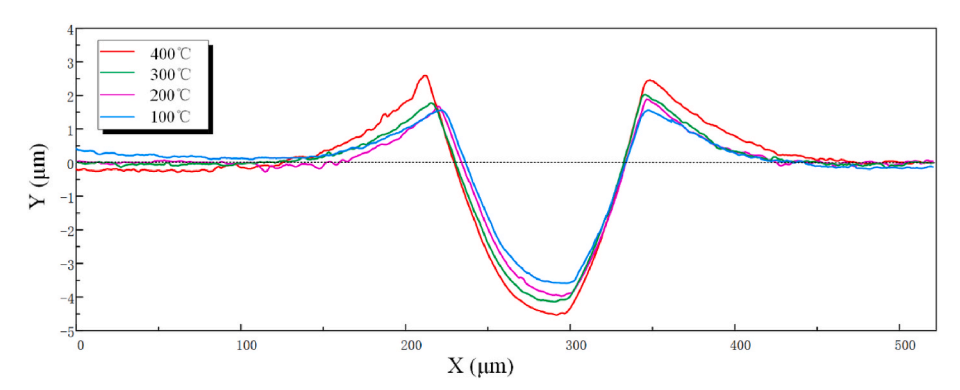


Fig. 17. Comparison of the depth of plastic-brittle transition of zirconia ceramics at different temperatures under the same scratch speed (6 mm/min).

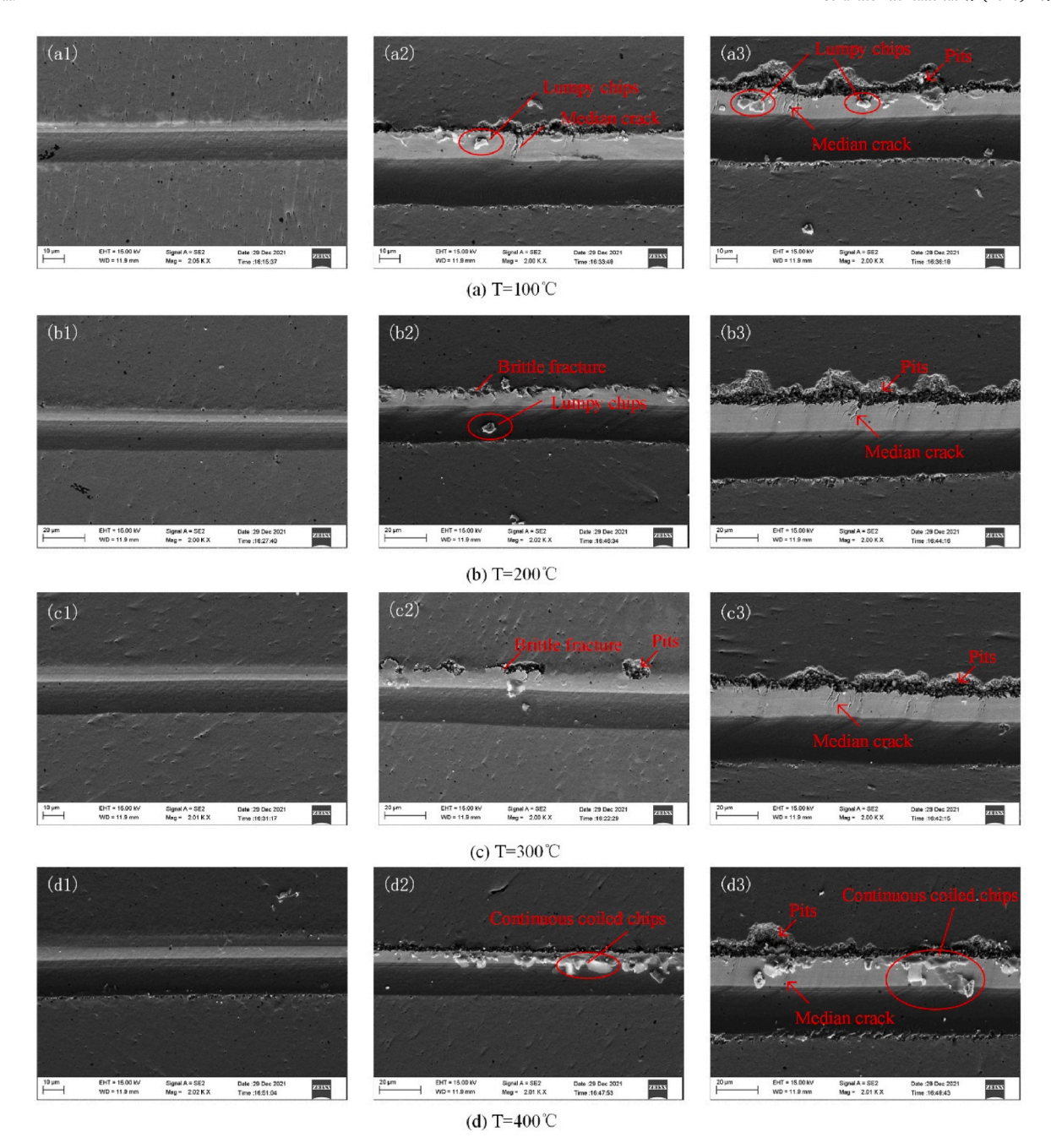


Fig. 18. SEM image of scratch morphology of zirconia ceramics at different temperatures.

indicating that plastic flow occurs more easily in zirconia ceramics. In the plastic-brittle transition stage, there are no obvious pits on both sides of the scratch, only a small amount of slight fracture. It is worth noting that the shape of removed zirconia ceramics changed from discontinuous lumpy chips to continuous coiled chips (see Fig. 18d2). In the brittle fracture stage, although pits and median cracks still exist, their number and size have been greatly reduced (see Fig. 18d3).

Based on the above phenomena, it can be considered that if the surface temperature of the ceramic is raised, the zirconia ceramics can be changed from the original brittle removal mode to the plastic removal mode, and the median cracks remaining inside the material would be suppressed, the broken pits at the edge of the processing zone is also reduced. What's more, the original lumpy chips were turned into continuous coiled chips, which further proves that plastic removal becomes the main removal method during heat-assisted machining.

## 5. Conclusion

- (1) Based on the heat conduction theory and Green's function, a mathematical model of temperature distribution on the surface of zirconia ceramics by laser beam is established. Through the combination of temperature measurement experiment and simulation calculation, the measured temperature field and the simulated temperature field are compared. The laser energy absorption rate of zirconia ceramics to the fiber laser is obtained, and the absorption rate value is 0.52.
- (2) Through nanoindentation tests, it is found that the elastic recovery rate of zirconia ceramics decreases with the increase of the load at room temperature. When the normal load exceeds 200 mN, cracks begin to appear at the boundary of the indentation zone. Through high temperature nanoindentation experiments, it is found that the elastic recovery rate of zirconia ceramics

increases with the increase of temperature, and the hardness and elasticity modulus decrease with the increase of temperature. The functional relationship between temperature and hardness and elasticity modulus of zirconia ceramics was obtained by function fitting. This study reveals the mechanism by which thermal-assisted machining technology can improve the machinability of zirconia ceramics.

(3) In the scratch test, the increase of scratching speed cannot substantially change the plastic-brittle transition depth and removal form of zirconia ceramics. However, the increase in temperature of zirconia ceramics can increase the depth of its plastic-brittle transition, and the proportion of plastic removal is significantly increased. The chips are transformed from discontinuous lumpy chips to continuous coiled chips. This study provides theoretical support for the study of material removal methods during thermal-assisted machining of zirconia ceramics.

#### 6. Outlook

In this paper, the mechanism of laser-assisted machining only for zirconia ceramic is studied. The difficulty in the industrialization of laser-assisted machining is that different materials absorb different laser energy at different rates. Therefore, more materials should be studied so that the mechanism of laser-assisted machining can be revealed more clearly.

# Declaration of competing interest

The authors declare that they have no known competing financial interests or personal relationships that could have appeared to influence the work reported in this paper.

# Acknowledgments

The authors sincerely appreciate the financial support provided by the National Natural Science Foundation of China (No.52075088 and 52105175).

# References

- [1] M. Yang, C. Li, Y. Zhang, D. Jia, X. Zhang, Y. Hou, R. Li, J. Wang, Maximum undeformed equivalent chip thickness for ductile-brittle transition of zirconia ceramics under different lubrication conditions, Int. J. Mach. Tool Manufact. 122 (2017) 55–65, https://doi.org/10.1016/j.ijmachtools.2017.06.003.
- [2] Z. Yang, L. Zhu, B. Lin, G. Zhang, C. Ni, T. Sui, The grinding force modeling and experimental study of ZrO2 ceramic materials in ultrasonic vibration assisted grinding, Ceram. Int. (2019) 1–17, https://doi.org/10.1016/j. ceramint.2019.01.216.
- [3] J.R. Kelly, I. Denry, Stabilized zirconia as a structural ceramic: an overview, Dent. Mater. 24 (2008) 289–298, https://doi.org/10.1016/J.DENTAL.2007.05.005.
- [4] J. Han, F. Zhang, B. Van Meerbeek, J. Vleugels, A. Braem, S. Castagne, Laser surface texturing of zirconia-based ceramics for dental applications: a review, Mater. Sci. Eng. C 123 (2021), 112034, https://doi.org/10.1016/j. msec.2021.112034.
- [5] Z. Yang, L. Zhu, G. Zhang, C. Ni, B. Lin, Review of ultrasonic vibration-assisted machining in advanced materials, Int. J. Mach. Tool Manufact. 156 (2020), 103594, https://doi.org/10.1016/j.ijmachtools.2020.103594.
- [6] C. Xiao, F.C. Hsia, A. Sutton-Cook, B. Weber, S. Franklin, Polishing of polycrystalline diamond using synergies between chemical and mechanical inputs: a review of mechanisms and processes, Carbon N Y 196 (2022) 29–48, https://doi. org/10.1016/j.carbon.2022.04.028.
- [7] Y. Hong, C. Sun, S. Xiu, C. Xu, L. Ma, X. Zou, Strengthening surface generation mechanism of carburizing-assisted grinding, Tribol. Int. (2023), 108300, https://doi.org/10.1016/J.TRIBOINT.2023.108300.

- [8] Z. Zhang, Y. Zhang, W. Ming, Y. Zhang, C. Cao, G. Zhang, A review on magnetic field assisted electrical discharge machining, J. Manuf. Process. 64 (2021) 694–722, https://doi.org/10.1016/j.jmapro.2021.01.054.
- [9] M. Yang, C. Li, Y. Zhang, D. Jia, R. Li, Y. Hou, H. Cao, J. Wang, Predictive model for minimum chip thickness and size effect in single diamond grain grinding of zirconia ceramics under different lubricating conditions, Ceram. Int. 45 (2019) 14908–14920, https://doi.org/10.1016/J.CERAMINT.2019.04.226.
- [10] M. Yang, C. Li, Y. Zhang, D. Jia, R. Li, Y. Hou, H. Cao, Effect of friction coefficient on chip thickness models in ductile-regime grinding of zirconia ceramics, Int. J. Adv. Manuf. Technol. 102 (5) (2019) 2617–2632, https://doi.org/10.1007/ S00170-019-03367-0, 102 (2019).
- [11] D. Jia, C. Li, Y. Zhang, M. Yang, X. Zhang, R. Li, H. Ji, Experimental evaluation of surface topographies of NMQL grinding ZrO2 ceramics combining multiangle ultrasonic vibration, Int. J. Adv. Manuf. Technol. 100 (2019) 457–473, https://doi. org/10.1007/S00170-018-2718-Y/METRICS.
- [12] K. You, G. Yan, X. Luo, M.D. Gilchrist, F. Fang, Advances in laser assisted machining of hard and brittle materials, J. Manuf. Process. 58 (2020) 677–692, https://doi.org/10.1016/j.jmapro.2020.08.034.
- [13] J.C. Rozzi, F.E. Pfefferkorn, F.P. Incropera, Y.C. Shin, Transient thermal response of a rotating cylindrical silicon nitride workpiece subjected to a translating laser heat source, Part I: comparison of surface temperature measurements with theoretical results, J. Heat Tran. 120 (1998) 899–906, https://doi.org/10.1115/1.2825909.
- [14] J.C. Rozzi, F.E. Pfefferkorn, F.P. Incropera, Y.C. Shin, Transient, three-dimensional heat transfer model for the laser assisted machining of silicon nitride: I. Comparison of predictions with measured surface temperature histories, Int. J. Heat Mass Tran. 43 (2000) 1409–1424, https://doi.org/10.1016/S0017-9310(99) 00217-3.
- [15] F.E. Pfefferkorn, F.P. Incropera, Y.C. Shin, Heat transfer model of semi-transparent ceramics undergoing laser-assisted machining, Int. J. Heat Mass Tran. 48 (2005) 1999–2012, https://doi.org/10.1016/j.ijheatmasstransfer.2004.10.035.
- [16] D. Kalyanasundaram, P. Shrotriya, P. Molian, Fracture mechanics-based analysis for hybrid laser/waterjet (LWJ) machining of yttria-partially stabilized zirconia (Y-PSZ), Int. J. Mach. Tool Manufact. 50 (2010) 97–105, https://doi.org/10.1016/j. ijmachtools.2009.09.002.
- [17] H. Ding, Y.C. Shin, Laser-assisted machining of hardened steel parts with surface integrity analysis, Int. J. Mach. Tool Manufact. 50 (2010) 106–114, https://doi. org/10.1016/j.jimachtools.2009.09.001.
- [18] G. Ren, H. Song, J. Dan, J. Li, P. Pan, Z. Yang, J. Xiao, J. Xu, Thermal analysis and machinability for laser-assisted machining of fused silica, Int. J. Heat Mass Tran. 148 (2020), https://doi.org/10.1016/j.ijheatmasstransfer.2019.119078.
- [19] T. Kizaki, Y. Ito, S. Tanabe, Y. Kim, N. Sugita, M. Mitsuishi, Laser-assisted machining of zirconia ceramics using a diamond bur, Procedia CIRP 42 (2016) 497–502, https://doi.org/10.1016/j.procir.2016.02.239.
- [20] Y. Guo, X. Yang, J. Kang, M. Li, Q. Xie, J. Xiao, W. Zhang, Experimental investigations on the laser-assisted machining of single crystal Si for optimal machining, Opt Laser. Technol. 141 (2021), 107113, https://doi.org/10.1016/j. optlastec.2021.107113.
- [21] C. Zhai, J. Xu, Y. Hou, G. Sun, B. Zhao, H. Yu, Effect of fiber orientation on surface characteristics of C/SiC composites by laser-assisted machining, Ceram. Int. 48 (2022) 6402–6413, https://doi.org/10.1016/J.CERAMINT.2021.11.183.
- [22] C. Wu, T. Zhang, W. Guo, X. Meng, Z. Ding, S.Y. Liang, Laser-assisted grinding of silicon nitride ceramics: micro-groove preparation and removal mechanism, Ceram. Int. 48 (2022) 32366–32379, https://doi.org/10.1016/J. CERAMINT.2022.07.180.
- [23] C. Li, Y. Hu, F. Zhang, Y. Geng, B. Meng, Molecular dynamics simulation of laser assisted grinding of GaN crystals, Int. J. Mech. Sci. 239 (2023), 107856, https://doi.org/10.1016/J.IJMECSCI.2022.107856.
- [24] Z. Ma, Z. Wang, X. Wang, T. Yu, Effects of laser-assisted grinding on surface integrity of zirconia ceramic, Ceram. Int. 46 (2020) 921–929, https://doi.org/ 10.1016/j.ceramint.2019.09.051.
- [25] Z. Ma, Q. Wang, H. Chen, L. Chen, S. Qu, Z. Wang, T. Yu, A grinding force predictive model and experimental validation for the laser-assisted grinding (LAG) process of zirconia ceramic, J. Mater. Process. Technol. 302 (2022), 117492, https://doi.org/10.1016/j.jmatprotec.2022.117492.
- [26] Z. Ma, Q. Wang, H. Chen, L. Chen, F. Meng, X. Chen, S. Qu, Z. Wang, T. Yu, Surface prediction in laser-assisted grinding process considering temperature-dependent mechanical properties of zirconia ceramic, J. Manuf. Process. 80 (2022) 491–503, https://doi.org/10.1016/j.jmapro.2022.06.019.
- [27] T.G. Bifano, T.A. Dow, R.O. Scattergood, Ductile-Regime grinding: a new technology for machining brittle materials, Journal of Manufacturing Science and Engineering, Transactions of the ASME 113 (1991) 184–189, https://doi.org/ 10.1115/1.2899676.
- [28] C. Li, Y. Piao, F. Zhang, Y. Zhang, Y. Hu, Y. Wang, Understand anisotropy dependence of damage evolution and material removal during nanoscratch of MgF2 single crystals, International Journal of Extreme Manufacturing 5 (2022), 015101, https://doi.org/10.1088/2631-7990/AC9EED.